Super Duplex Stainless Steel

Subjects: Ergonomics
Contributor: ANNA NOCIVIN

In this present study, the influence of isothermal aging temperature and duration on microstructural and mechanical properties of a hot-deformed UNS S32750 Super Duplex Stainless Steel (SDSS) alloy was investigated by SEM-EBSD (Scanning Electron Microscopy-Electron Backscatter Diffraction) and tensile testing techniques. An isothermal aging treatment, at temperatures between (400 - 600)°C and treatment duration between (3 - 120)h, was applied to a commercial UNS S32750 SDSS alloy. Microstructural characteristics of all thermo-mechanical (TM) processed states, such as distribution and morphology of constituent phases, grain's modal orientation (MO) and, obtained mechanical properties were analysed correlated with the TM processing conditions. Obtained experimental results show that the constituent phases, in all TM processed states, are represented by delta- and gamma-phases. SEM-EBSD analysis revealed microstructural modifications induced by TM processing, showing elongated gamma-phase grains within delta-phase matrix. Within the delta-phase matrix, dynamically recrystallized grains were identified as a result of applying hot deformation and isothermal aging treatments. Also, it was observed that aging treatment parameters can significantly influence the mechanical behaviour exhibited by the UNS S32750 SDSS alloy, in terms of elongation to fracture and absorbed energy during impact testing.

Keywords: Super-Duplex Stainless Steel (SDSS) ; gamma-Fe (austenite) ; delta-Fe (ferrite) ; sigma-phase ; microstructure ; mechanical properties

1. Materials and Methods

The investigated UNS S32750 super duplex stainless steel (SDSS) alloy was thermo-mechanically (TM) processed according to the processing route presented in Figure 1. The as-received (AR) UNS S32750 alloy was hot deformed by rolling (hot-rolled—HR), at a temperature of 1100 °C, using six rolling steps, up to a total deformation degree (thickness reduction) of approximately $\varepsilon_{total} \approx 65\%$. For each rolling step, a constant deformation degree ($\varepsilon_{partial} \approx 11\%$) was used. After each rolling step, the rolled samples were re-heated up to the nominal deformation temperature (1100 °C) in order to perform the next rolling step.

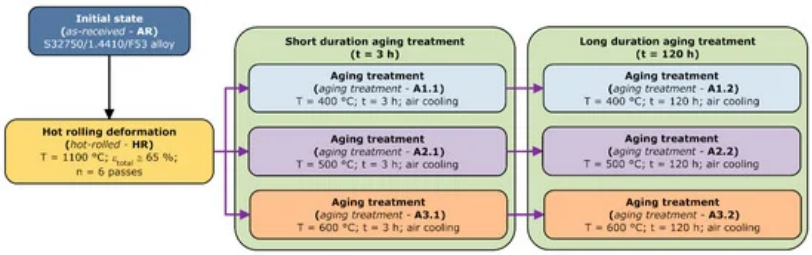

Figure 1. Schematic representation of the applied thermomechanical processing route.

After hot rolling, the samples were aged using different temperatures and durations. The first set of samples was subjected to *short-duration aging treatments*, at the following temperatures: 400 °C (*aging treatment-A1.1*), 500 °C (*aging treatment-A2.1*), and 600 °C (*aging treatment-A3.1*), with a duration of 3 h (180 min). The second set of samples was subjected to *long-duration aging treatments*, at the following temperatures: 400 °C (*aging treatment-A1.2*), 500 °C (*aging treatment-A2.2*), and 600 °C (*aging treatment-A3.2*), with a duration of 120 h (five days).

All TM processed specimens were investigated from the point of view of microstructural and mechanical properties. Considering the TM processing specific features, the samples´ reference frame, indicated in Figure 2a, assumes the following main directions: *RD—rolling direction*, *TD—transverse direction*, and *ND—normal direction*. The sample's microstructure was analysed in the plane defined by the RD–ND directions, while all mechanical properties were analysed along the RD direction (Figure 2b).

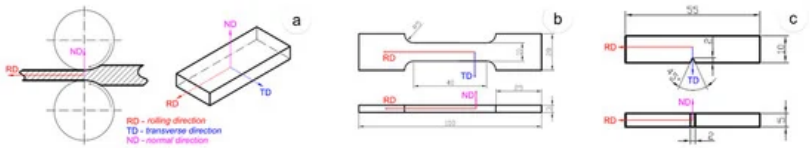

Figure 2. Samples reference system (**a**), geometrical configuration for tensile testing (**b**), and Charpy testing specimens (**c**).

The metallographic preparation procedure applied to all the samples collected from all TM processed states is presented and detailed elsewhere [1][2][3]. The microstructure was investigated by SEM techniques, with the purpose of observing the microstructural constituent phases and the changes occurred during TM processing. A SEM-TESCAN Vega II-XMU (TESCAN, Brno, Czech Republic) microscope was used to perform microstructural analysis.

Microstructural constituent phases and changes occurred during TM processing were analysed using the SEM coupled with a BRUKER Quantax e-Flash EBSD detector. The following parameters were used: 250× magnification, 320 × 240 pixels resolution, 10 ms acquisition time/pixel, 1 × 1 binning size, and less than 3% zero solutions. During the SEM-EBSD analysis, the identified phases were indexed as follows: δ-phase indexed in body-centred cubic (BCC) system, with a lattice parameter of a = 2.86 Å; γ-phase indexed in face-centred cubic (FCC) system, with a lattice parameter of a = 3.66 Å; and R-phase (Fe(Cr)NiMo) indexed in the trigonal system, with a lattice parameter of a = 10.85 Å and c = 19.71 Å. No other secondary phases (i.e., χ-phase, σ-phase, nitrides, carbides) were detected during SEM-EBSD analysis.

All TM processed specimens were also tensile tested in order to determine the following mechanical properties: ultimate tensile strength (σ_{UTS}), 0.2 yield strength ($\sigma_{0.2}$), and elongation to fracture (ε_f). For tensile testing, the dog-bone shaped samples were used (Figure 2b), with a calibrated section of 40 mm × 10 mm × 3 mm. Further, during testing, a 12.5 mm displacement extensometer was used. Tensile testing measurements were performed using an INSTRON 3382 (INSTRON, Norwood, MA, USA) universal testing equipment. Besides tensile testing, an impact Charpy testing was performed using V-notch 55 mm × 10 mm × 5 mm samples (Figure 2c). The Charpy testing measurements were performed using an INSTRON 450 MPX-v2-J1 (INSTRON, Norwood, MA, USA) testing equipment. In order to compute the average values for all investigated mechanical properties, the following procedure was applied: for each TM processed specimen, six arbitrary samples were tested in identical conditions; computed data were statistically analysed and the standard deviation was determined for each investigated mechanical property. All data were rounded to the nearest whole number, in MPa and J (for strength and impact properties), while the elongation was rounded to 0.5% (i.e., according to EN 10002-1).

2. Results

2.1. Microstructural Evolution During TM Processing of UNS S32750 SDSS Alloy

Figure 3a shows the SEM-EBSD image of phase map distribution for the UNS S32750 SDSS alloy in the as-received (AR) state. One can observe that the identified phases were as follows: δ-phase (coloured in blue) and γ-phase (coloured in red). One can also observe that the γ-phase presents an islands-like morphology within the δ-phase matrix. On the basis of SEM-EBSD analysis, the constituent phase ratio was computed. The computation algorithm assumed 10 measurements of 403.4 × 403.4 (μm × μm) fields and statistical analysis of obtained phase ratios. It was determined that the F53 SDSS alloy in AR condition showed the presence of 49.1% ± 2.3% δ-phase and 50.9% ± 2.1% γ-phase. Figure 3b shows the grains' orientation distribution for both the δ-phase and γ-phase. A closer look at the γ-phase grains' orientation distribution shows the presence of annealing twins. Similar observations were also made by other researchers, showing that the annealing twins belong to the {111} <112> system [4][5][6].

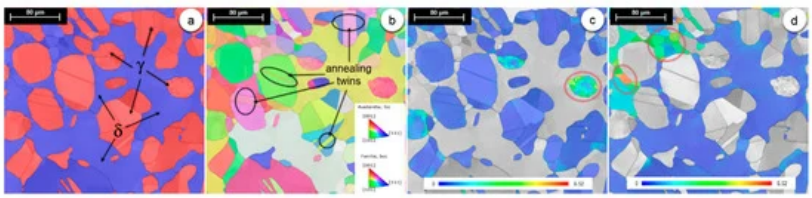

Figure 3. Distribution map of the γ- and δ-phases (**a**), inverse pole figure (IPF) (**b**), grain reference orientation deviation (GROD) map of γ-phase (**c**) and δ-phase (**d**) for the *as-received* (*AR*) state.

The grain reference orientation deviation (GROD) map can be used as a visualisation tool to assess the accumulated deformation/strain at microstructural level [7][8]. GROD is based on the misorientation (MO) between a reference point of that grain and the other points. The reference point can be the mean orientation of the grain or the point of the grain where the KAM (kernel average misorientation) is the lowest [9][10]. In the present work, the GROD map provides the orientation field referenced to a fixed point, which is the mean orientation of the grain. As shown, the GROD map shows grains exhibiting deviations from the average grain orientation, deviations due to accumulated strain resulting as a consequence of, firstly, grains' deformations by slip/twinning and/or rotations and, secondly, other induced strain hardening effects during applied TM processing. Figure 3c,d show the GROD maps for the γ-phase and δ-phase, respectively. One can observe that the maximum MO reaches a value close to 6.52° and is recorded in the case of the δ-phase (Figure 3d). The γ-phase shows grains with a level of accumulated strain inferior to δ-phase, and in both phases, the maximum level of MO is recorded in small-size grains (Figure 3c,d).

Figure 4a shows the phase map distribution for the hot-rolled (HR) state. The microstructure consists of the δ-phase (coloured in blue) and γ-phase (coloured in red). It can be observed that the γ-phase shows a modified morphology, from an islands-like to a typical roll-deformed one, with high-elongated grains, along the RD direction, within the δ-phase matrix. Analysing the grains' orientation distribution for both the δ-phase and γ-phase (Figure 4b), one can observe that the γ-phase grains accommodate better induced intense deformation, during the hot-deformation processing, when compared with the δ-phase grains and, furthermore, the observed annealing γ-phase twins show signs of deformation. Figure 4c,d show the GROD maps for the γ-phase and δ-phase, respectively. One can observe that the maximum MO reaches a value close to 31.62° (an increase of approximately 485%, compared with the AR state) and is recorded in the case of the δ-phase (Figure 4d). Besides intensely deformed grains, the δ-phase shows the presence of new dynamically recrystallized grains, which show uniform GROD distribution, with an average MO close to 0°, and an average grain-size close to 30 μm (Figure 4d). No new dynamically recrystallized grains were observed in the case of the γ-phase.

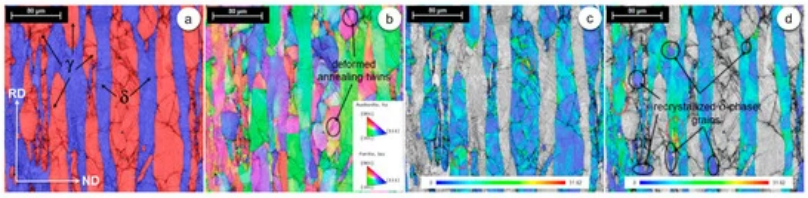

Figure 4. Distribution maps of both the γ- and δ-phases (**a**), inverse pole figure (IPF) (**b**), GROD map of the γ-phase (**c**) and δ-phase (**d**) for the *hot-rolled* (*HR*) state.

In all aging treatments states, short-duration aging treatments—A1.1, A2.1, and A3.1 states—and long-duration aging treatments—A1.2, A2.2, and A3.2 states—the observed morphology of both the δ-phase and γ-phase shows the same typical roll-deformed features, with highly-elongated, along the RD direction, γ-phase grains within the δ-phase matrix (Figure 5a,e, Figure 6a,e, Figure 7a,e). Only in the case of long-duration aging treatment A2.3, besides the δ-phase and γ-phase, a precipitated secondary phase was detected, namely the R-phase (Fe(Cr)NiMo) (Figure 7e), showing a fine and almost uniform distribution within the δ-phase matrix. The computed R-phase weight fraction, based on EBSD data, is situated close to 6.5%. In all cases, grains' orientation distribution, for the δ-phase and γ-phase, shows that the γ-phase grains accommodate better the intense deformation compared with the δ-phase grains and the annealing γ-phase twins are still present (Figure 5b,f, Figure 6b,f, Figure 7b,f). Significant differences were observed in the case of GROD maps. One can see that the maximum GROD decreases continuously with the increasing aging treatment temperature and duration. In all cases, the maximum MO is recorded for the δ-phase. In the case of short-duration aging treatment states, the maximum MO continuously decreases to 20.40° for the A1.1 state (Figure 5d) (a decrease of approximately 35.5% compared with the HR state), to 17.80° for the A2.1 state (Figure 6d) (a decrease of approximately 43.7% compared with the HR state), and finally to 15.11° for the A3.1 state (Figure 7d) (a decrease of approximately 52.2% compared with the HR state). Analysing the case of long-duration aging treatment states, it can be observed that the GROD maps suffers further decreasing owing to increased treatment duration (120 h). Recorded maximum MO values are continuously decreasing, to 18.50° for the A1.2 state (Figure 5h) (a decrease of approximately 9.3% compared with the A1.1 state), to 16.20° for the A2.2 state (Figure 6h) (a decrease of approximately 8.9% compared with the A2.1 state), and finally to 13.8° for the A3.2 state (Figure 7h) (a decrease of approximately 8.6% compared with the A3.1 state). The observed decrease suggests that an important effect induced by the aging treatments is represented by the stress relieving phenomena within the microstructure. The main characteristics of stress relieving are represented by the removal of unwanted effects induced by plastic deformation. Owing to stress relieving, the crystal imperfections density and high elastic strains and residual stress fields can be significantly lowered, improving the material's exhibited properties.

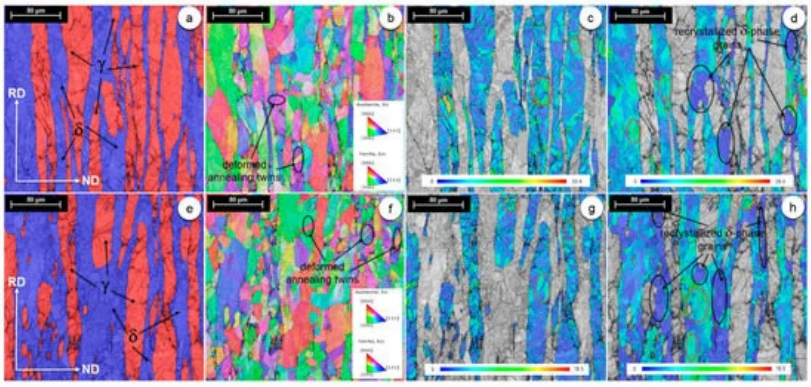

Figure 5. Distribution maps of both the γ- and δ-phases (**a**), inverse pole figure (IPF) (**b**), GROD map of the γ-phase (**c**) and δ-phase (**d**) for the *short-duration aging treatment* (*A1.1*) state; distribution maps of both the γ- and δ-phases (**e**), inverse pole figure (IPF) (**f**), GROD map of the γ-phase (**g**) and δ-phase (**h**) for the *long-duration aging treatment* (*A1.2*) state.

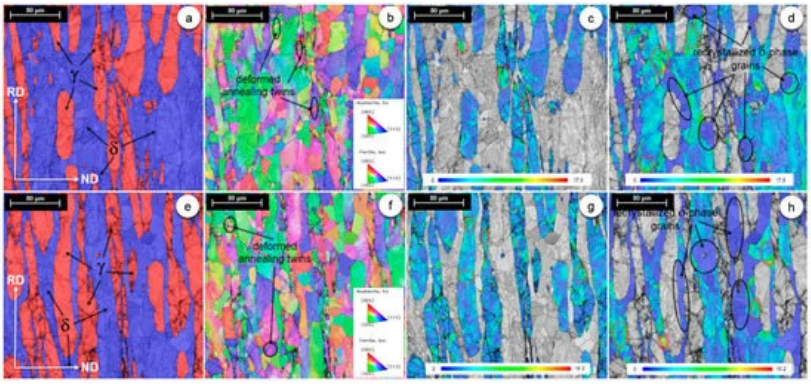

Figure 6. Distribution maps of both the γ- and δ-phases (**a**), inverse pole figure (IPF) (**b**), GROD map of the γ-phase (**c**) and δ-phase (**d**) for the *short-duration aging treatment* (*A2.1*) state; distribution maps of both the γ- and δ-phases (**e**), inverse pole figure (IPF) (**f**), GROD map of the γ-phase (**g**) and δ-phase (**h**) for the *long-duration aging treatment* (*A2.2*) state.

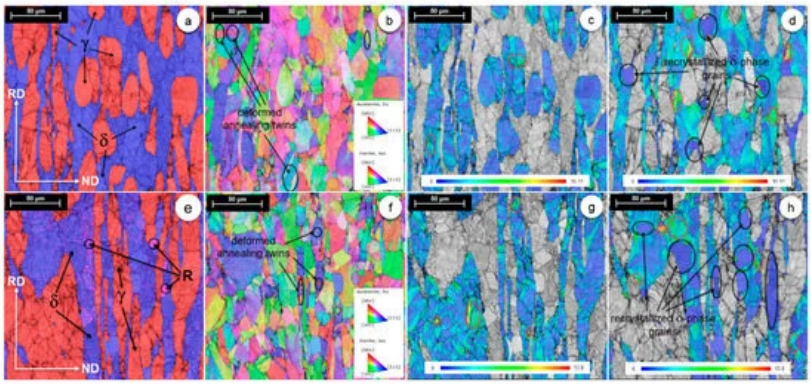

Figure 7. Distribution maps of both the γ- and δ-phases (**a**), inverse pole figure (IPF) (**b**), GROD map of the γ-phase (**c**) and δ-phase (**d**) for the *short-duration aging treatment* (*A3.1*) state; distribution maps of both the γ- and δ-phases (**e**), inverse pole figure (IPF) (**f**), GROD map of the γ-phase (**g**) and δ-phase (**h**) for the *long-duration aging treatment* (*A3.2*) state.

In both short-duration aging treatment and long-duration aging treatment states, one can observe the presence of new, dynamically recrystallized δ-phase grains. If one compares the observed number of recrystallized δ-phase grains in the case of HR (Figure 4d) with ones obtained after aging performed at 400 °C for 3 h (A1.1 state—Figure 5d) and 120 h (A1.2 state—Figure 5h), they will notice that the highest number of recrystallized δ-phase grains is observed in the case of the A1.2 state, followed by the A1.1 state, and finally the HR state, suggesting that the aging treatment duration influences the recrystallization of new δ-phase grains. Similar observations can also be made in the case of aging performed at 500 °C for 3 h (A2.1 state—Figure 6d) and 120 h (A2.2 state—Figure 6h), and in the case of aging performed at 600 °C for 3 h (A3.1 state—Figure 7d) and 120 h (A3.2 state—Figure 7h). Generally, an intensely deformed phase behaves better as the number of new recrystallized grains, from the parent phase, is increasing (i.e., if one considers δ-phase ductility, it is expected that a higher ductility will be obtained as the number of recrystallized grains is increasing).

The decrease in GROD and the increased number of recrystallized δ-phase grains are proving that aging treatments, at temperatures between 400 and 600 °C and durations between 3 and 120 h, can influence the properties exhibited by the UNS S32750 SDSS alloy.

References

1. Cerenis Therapeutics, S. Cer-001 Therapy as a Novel Approach to Treat Genetic Orphan Diseases (TANGO). Available online: ClinicalTrials.gov/ct2/show/NCT02697136 (accessed on 11 February 2019).
2. David O. Osei-Hwedieh; Marcelo Amar; Dmitri Sviridov; Alan T Remaley; Apolipoprotein mimetic peptides: Mechanisms of action as anti-atherogenic agents. *Pharmacology & Therapeutics* **2010**, *130*, 83-91, 10.1016/j.pharmthera.2010.12.003.
3. Shuo Yang; Marina G. Damiano; Heng Zhang; Sushant Tripathy; Andrea J. Luthi; Jonathan S. Rink; Andrey V. Ugolkov; Amareshwar T. K. Singh; Sandeep S. Dave; Leo I. Gordon; et al. Biomimetic, synthetic HDL nanostructures for lymphoma. *Proceedings of the National Academy of Sciences* **2013**, *110*, 2511-2516, 10.1073/pnas.1213657110.
4. Yue Yuan; Jian Wen; Jie Tang; Qiming Kan; Rose Ackermann; Karl Olsen; Anna Schwendeman; Synthetic high-density lipoproteins for delivery of 10-hydroxycamptothecin. *International Journal of Nanomedicine* **2016**, *11*, 6229, 10.2147/IJN.S112835.
5. Chitra Subramanian; Rui Kuai; Qing Zhu; Peter White; James J. Moon; Anna Schwendeman; Mark S. Cohen; Synthetic high-density lipoprotein nanoparticles: A novel therapeutic strategy for adrenocortical carcinomas.. *Surgery* **2016**, *159*, 284-294, 10.1016/j.surg.2015.08.023.
6. Rui Kuai; Chitra Subramanian; Peter T White; Barbara N Timmermann; James J. Moon; Mark S Cohen; Anna Schwendeman; Synthetic high-density lipoprotein nanodisks for targeted withalongolide delivery to adrenocortical carcinoma. *International Journal of Nanomedicine* **2017**, *12*, 6581, 10.2147/IJN.S140591.
7. Emily E. Morin; Xiang-An Li; Anna Schwendeman; HDL in Endocrine Carcinomas: Biomarker, Drug Carrier, and Potential Therapeutic. *Frontiers in Endocrinology* **2018**, *9*, 715, 10.3389/fendo.2018.00715.
8. Ji Wang; Junting Jia; Jianping Liu; Hongliang He; Wenli Zhang; Zhenghua Li; Tumor targeting effects of a novel modified paclitaxel-loaded discoidal mimic high density lipoproteins. *Drug Delivery* **2013**, *20*, 356-363, 10.3109/10717544.2013.834418.
9. Jose Medina-Echeverz; Marcos Vasquez; Celia Gomar; Nuria Ardaiz; Pedro Berraondo; Overexpression of apolipoprotein A-I fused to an anti-transforming growth factor beta peptide modulates the tumorigenicity and immunogenicity of mouse colon cancer cells. *Cancer Immunology, Immunotherapy* **2015**, *64*, 717-725, 10.1007/s00262-015-1681-9.
10. Linda K. Mooberry; Maya Nair; Sulabha Paranjape; Walter J. McConathy; Andras G Lacko; Receptor mediated uptake of paclitaxel from a synthetic high density lipoprotein nanocarrier. *Journal of Drug Targeting* **2010**, *18*, 53–58, 10.1080/10611860903156419.